Rotating spintronic terahertz emitter optimized for microjoule pump-pulse energies and megahertz repetition rates

View Online   Export Citation   CrossMark

Alkisti Vaitsi,[1] Vivien Sleziona,[1] (iD) Luis E. Parra López,[1] (iD) Yannic Behovits,[2] (iD) Fabian Schulz,[1,3] (iD)
Natalia Martín Sabanés,[1,4] (iD) Tobias Kampfrath,[1,2] (iD) Martin Wolf,[1] (iD) Tom S. Seifert,[2] (iD) and Melanie Müller[1,a)] (iD)

AFFILIATIONS

[1]Department of Physical Chemistry, Fritz Haber Institute of the Max Planck Society, 14195 Berlin, Germany
[2]Department of Physics, Freie Universität Berlin, 14195 Berlin, Germany
[3]CIC NanoGUNE, 20018 Donostia-San Sebastián, Spain
[4]IMDEA Nanoscience, 28049 Madrid, Spain

[a)]Author to whom correspondence should be addressed: m.mueller@fhi-berlin.mpg.de

ABSTRACT

Spintronic terahertz emitters (STEs) are powerful sources of ultra-broadband single-cycle terahertz (THz) field transients. They work with any pump wavelength, and their polarity and polarization direction are easily adjustable. However, at high pump powers and high repetition rates, STE operation is hampered by a significant increase in the local temperature. Here, we resolve this issue by rotating the STE at a few 100 Hz, thereby distributing the absorbed pump power over a larger area. Our approach permits stable STE operation at a fluence of $\sim$1 mJ/cm^2 with up to 18 W pump power at megahertz repetition rates, corresponding to pump-pulse energies of a few 10 μJ and pump power densities approaching 1 kW/cm^2. The rotating STE is of interest for all ultra-broadband high-power terahertz applications requiring high repetition rates. As an example, we show that terahertz pulses with peak fields of 10 kV/cm can be coupled to a terahertz-light wave-driven scanning tunneling microscope at 1 MHz repetition rate, demonstrating that the rotating STE can compete with standard terahertz sources such as LiNbO$_3$.

Spintronic terahertz (THz) emitters (STEs) have emerged as versatile sources of ultra-broadband single-cycle terahertz pulses without spectral gaps,[1] delivering peak electric fields up to $\sim$1 MV/cm.[2,3] Among other advantages,[4,5] STEs offer easy and versatile polarity and polarization control via external magnetic fields,[6–8] wavelength-independent excitation[9] without phase matching constraints, excellent beam quality and focusability,[2] and Fourier-limited single-cycle transients with ultra-wide bandwidth.[1] Therefore, they are of particular interest for terahertz field-driven applications such as terahertz-light wave scanning tunneling microscopy (THz-STM)[10–12] and field-resolved terahertz scanning near-field optical microscopy (THz-SNOM).[10,13] A crucial aspect for these applications is the generation of measurable terahertz-field-induced currents or scattered terahertz near-field signals, which requires operation at megahertz repetition rates and sufficiently high terahertz field strength, e.g., up to few kilovolts per cm in the case of THz-STM.[10,14,15] Modern Yb-based high-power femtosecond laser

systems[16–18] combined with external pulse compressors[19–22] provide pulses with a duration down to a few 10 fs at several 10–100 W of output power and megahertz repetition rates, motivating the optimization of broadband terahertz sources such as the STE at such laser parameters.[23–27] This will further pave the way for future technological applications in broadband terahertz imaging,[28,29] sensing, and spectroscopy that will greatly benefit from high terahertz powers.

To exploit the full potential of STEs for terahertz-field-driven applications, the conversion of optical energy into emitted terahertz field (optical-to-terahertz-field conversion efficiency, FCE) as well as the propagation and focusing of the broadband terahertz pulses in the experiment must be optimized. Optimal FCE of the STE is typically achieved by exciting the STE at a pump fluence of $\sim$1 mJ/cm^2.[2,23] However, at pump powers of several 10 W and megahertz repetition rates, accumulated heating over many laser pulses can significantly reduce the FCE and even lead to irreversible degradation or immediate

damage of the STE.[23] Excitation of the STE with pump spot sizes of several centimeters, as shown for multi-Watt operation at kilohertz repetition rates,[2,3] minimizes heating and results in an optimal FCE at millijoule pump-pulse energies. However, at megahertz repetition rates and few 10 μJ pulse energies, this approach will result in very low fluence and correspondingly reduced FCE. On the other hand, if the fluence is increased by decreasing the pump spot size, the elevated power density and resulting significant heating will limit STE operation to low pump powers. Thus, achieving a fluence of 1 mJ/cm^2 at megahertz repetition rates and multi-Watt average powers is a major challenge and requires efficient heat management. Active backside cooling of the STE was demonstrated recently,[23] but it requires operation in a backreflection geometry that is less straightforward than a transmission geometry. In addition, the maximum usable power will be limited by heat transport within the cooled STE device, and scaling to higher powers will require complex cryogenic environments.

Here, we demonstrate efficient high-power operation of a trilayer STE excited at megahertz repetition rates with up to 18 W chopped pump power and pump spot sizes of a few millimeters, resulting in a fluence of $\sim$1 mJ/cm^2 and power densities as high as several 100 W/cm^2. This is achieved by rotating the STE at an angular speed of 100–300 Hz, which effectively reduces the locally accumulated heat by distributing the absorbed power over an area much larger than the excitation spot. In addition to the actual terahertz generation process, achieving high terahertz electric fields in an experiment requires an optimal terahertz-beam guiding. Accordingly, we optimize the collimation, propagation, and focusing of the terahertz beam generated by the rotating STE. This procedure allows us to generate 10 kV/cm peak incident terahertz fields at the tip of a low-temperature STM, resulting in several volts peak terahertz bias between the STM tip and a metallic sample.

Figure 1 shows the experimental setup. We excite the STE with 1030 nm near-infrared (NIR) pulses of $\sim$35 fs duration. The NIR pulses are generated by a high-power femtosecond laser (Light Conversion Carbide-80W), whose output pulses ($\sim$200 fs) are spectrally broadened and temporally compressed in a multi-plate compressor (MPC).[19,20,22]

The system offers two operating modes, providing either 50 or 20 μJ of compressed NIR pulse energy at 1 MHz or 2 MHz repetition rate. Part of the NIR power is split off for use as sampling pulses in electro-optic sampling (EOS) or for phase-resolved terahertz waveform sampling in the STM.[11,30] A large-area STE of 2″ diameter on 500 μm sapphire (TeraSpinTec GmbH) is excited at a radial position $r_p = 20$ mm from its center under normal incidence. The diameter $2w_p$ (1/e^2 intensity width) of the collimated pump beam can be varied between 1.7, 2, and 3.7 mm by using different lenses in the beam path. The NIR pump power P_p is controlled by a half-wave plate and a pair of thin-film polarizers. The STE is mounted on the shaft of a direct current (DC) motor that can rotate at a maximum frequency of $f_{rot} = 300$ Hz and is magnetized by a permanent magnet of 25 mm diameter, i.e., significantly larger than the pump spot size to ensure homogeneous magnetization of the excited region [see Fig. 2(a)]. The center axis of the magnet and, thus, the magnetization is directed toward the center of the STE so that the emitted terahertz pulses are linearly polarized along the direction perpendicular to the resulting sample magnetization.

A glass plate coated with indium-tin-oxide (ITO) is mounted closely behind the STE to separate the terahertz radiation from the residual pump beam. The reflected terahertz pulses are collected by a 90° off-axis parabolic mirror (OAPM), which is part of a telescope (1:6) to expand the terahertz beam. The distance between the STE and the first telescope mirror is minimized to $\sim$5 cm to minimize divergence of the generated terahertz beams. A germanium (Ge) wafer is installed at an angle of 55° to block the residual pump light. A second ITO-coated glass is used to overlap the sampling pulses collinearly with the terahertz beam. A flip mirror allows to send the terahertz beam either into the STM or to an identical beam path for EOS. In both cases, we focus the terahertz beam using a 90° OAPM with a diameter of 1″ and a focal length of 35 mm. EOS traces are recorded using a 300 μm-thick ZnTe(110) crystal and are deconvoluted with the detector response function to extract the terahertz electric field at the detector position.[31–33] The terahertz power emitted by the STE is measured by a pyroelectric detector (Gentec THZ9B-BL-DA) at the EOS
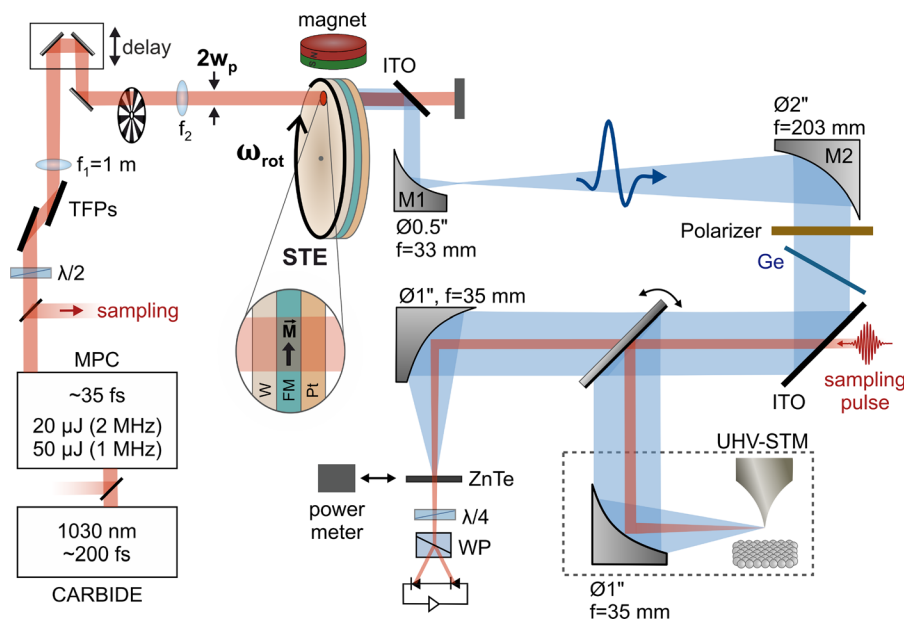

FIG. 1. Experimental setup. $\vec{M}$: magnetization, MPC: multi-plate compressor, TFP: thin film polarizer, ITO: indium tin oxide glass, ZnTe: zinc telluride crystal, WP: Wollaston prism, Ge: germanium wafer, UHV: ultrahigh vacuum, w_p: pump-beam radius. The focal length f_2 of the recollimation lens is 750, 500, and 400 mm for the three pump spot sizes, respectively.
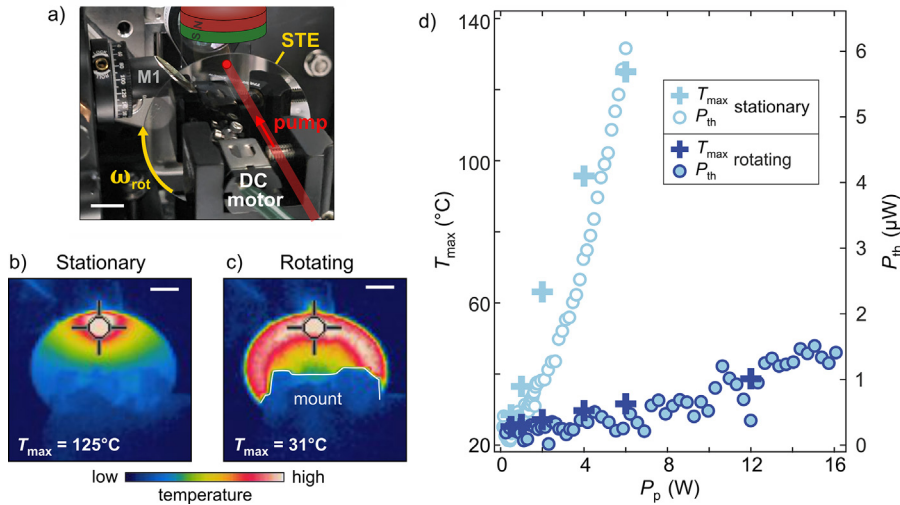
FIG. 2. (a) Photo of the mounting and excitation conditions of the rotating STE. (b) and (c) Spatial temperature profile of the stationary (b) and rotating (c) STE for $P_p = 6$ W. The peak temperature T_{max} is measured in the crosshairs. The color scales are saturated for better visibility of temperature gradients. The white line in (c) indicates the mount of the STE. (d) Steady-state peak temperature T_{max} and thermal radiation power P_{th} at the detector position ($f_{rep} = 2$ MHz, $f_{rot} = 300$ Hz, scale bars 1 cm).

position, for which the NIR beam and, thus, the terahertz beam are chopped at 5 Hz with a 50% duty cycle to allow lock-in detection. All given NIR powers are chopped values. Another Ge wafer is mounted on the terahertz power meter to block NIR background radiation. A terahertz polarizer is used to block the linearly polarized terahertz pulses to estimate the power of thermal radiation emitted by the STE. Details about the terahertz power calibration and the correction for transmission losses are explained in the supplementary material. Finally, we measure the temperature of the STE by a heat camera (Model FLIR InfraCAM SD).

First, we characterize the steady-state peak temperature T_{max} of the STE during stationary and rotating operation. Figure 2(b) shows a heat camera image of the stationary STE excited with $2w_p = 3.7$ mm at $P_p = 6$ W. The STE heats up to $T_{max} \approx 125\,°C$ in the center of the pump beam. Although the STE is not immediately damaged in this state, its efficiency decreases irreversibly within a few minutes, or several hours to days at lower powers in the range down to 1 W. Figure 2(c) shows the spatial distribution of T_{max} for the STE rotating at $f_{rot} = 300$ Hz. Remarkably, the peak temperature decreases significantly to $T_{max} \approx 31\,°C$. Moreover, the temperature increase is now distributed over a larger area, which is given by the annulus defined by r_p and $2w_p$ and the thermal transport in the film. Note that only a sector of the annulus is visible in Fig. 2(c) because the mount partially obscures the STE.

If we assume for simplicity that the temperature increase ΔT due to linear absorption scales linearly with the absorbed power density, we expect an inverse scaling with the illuminated area. From the ratio of $(\pi 2 r_p 2 w_p)/(\pi w_p^2) \approx 43$ of the areas of the annulus and the pump spot, the temperature increase should be reduced by a factor of ~ 43 when rotating the STE. At $P_p = 6$ W, T_{max} increases by $\Delta T_{stat} = 125\,°C - 22\,°C = 103\,°C$, and $\Delta T_{rot} = 31\,°C - 22\,°C = 9\,°C$ for the stationary and rotating STE, respectively. Therefore, the temperature increase is reduced by a factor of ~ 11.5 when rotating the STE, which is ~ 3.7 times smaller than the increase in area. This simple estimate neglects effects such as increased air cooling during rotation, heat transfer into the substrate, temperature-dependent material constants, or different volume-to-surface ratios of the excited areas. A detailed analysis of the cooling rates and steady-state temperature profile of the STE is beyond the scope of this work.

To further characterize the thermal properties of the STE, we measure the thermal radiation power P_{th} emitted by the STE that reaches the detector. Here, P_{th} is corrected by a factor 2 to account for the 50% loss at the polarizer to give the thermal power that reaches the sample in future experiments without the polarizer. A detailed explanation of the power calibration is provided in the supplementary material. Figure 2(d) shows P_{th} (right ordinate) and T_{max} (left ordinate) measured at $f_{rep} = 2$ MHz. For the stationary STE, P_{th} increases steeply and similar to T_{max}, where we limit the pump power to 6 W to avoid damaging the STE. Remarkably, T_{max} stays below 50 °C and P_{th} decreases considerably over the full power range. The results in Fig. 2 clearly show that moderately fast rotation efficiently reduces the average power heating of the STE.

Next, we analyze the dependence of the power $P_{THz,STE}$ of the coherent terahertz pulses emitted by the STE on P_p for different pump-beam sizes for the stationary and rotating STE, see Fig. 3(a). $P_{THz,STE}$ is corrected for thermal radiation and transmission losses through the setup (see the supplementary material). For the stationary STE (open markers), after an initial increase in the range $P_p \lesssim 1$ W, $P_{THz,STE}$ saturates and eventually decreases for higher pump powers. When the STE rotates, $P_{THz,STE}$ scales quadratically up to $P_p \approx 1$–2 W and continues to increase with a subquadratic dependence at higher powers. We find that the scaling starts to deviate from the expected quadratic dependence at a fluence of ~ 0.1 mJ/cm^2. This behavior is independent of the spot size, as shown together with quadratic fits to the data in the low power range plotted in the supplementary material, Fig. S3(b).

Moreover, at a given pump power, $P_{THz,STE}$ is higher for smaller pump beams due to the higher fluence and correspondingly higher optical-to-terahertz power conversion efficiency (PCE), as seen in Fig. 3(b) and as expected for a second-order nonlinear-optical process. The PCE saturates to values similar to those reported in previous work,[23] and a decrease in PCE is only observed for very high pump powers and fluences above ~ 1 mJ/cm^2 [see Fig. S4(a)]. Finally, Fig. 3(a) shows that the STE performance does not depend on f_{rot} between 100 and 300 Hz. This observation implies that lateral heat transport out of the illuminated area takes longer than one rotation, i.e., longer than 10 ms.
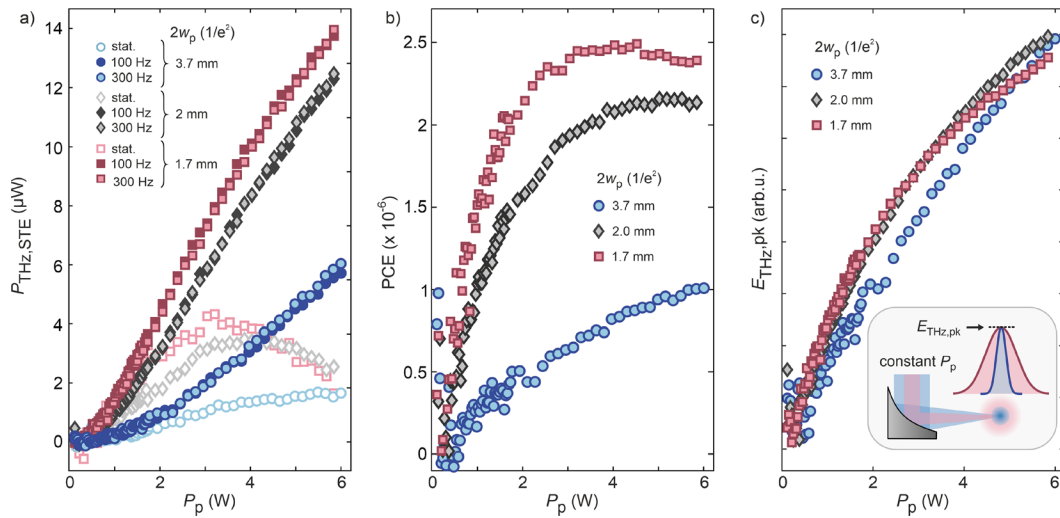
FIG. 3. (a) Terahertz power emitted by the stationary and rotating STE vs pump power for three pump spot sizes. Power conversion efficiency of the STE (b) and scaling of the peak terahertz electric field (c) vs pump power for $f_{rot} = 300$ Hz. Inset: illustration of constant terahertz peak field at constant pump power but varying pump spot size.($f_{rep} = 2$ MHz).

For field-driven applications such as THz-STM, the terahertz field is a more relevant quantity than the terahertz power. Figure 3(c) shows the pump-power scaling of the terahertz peak field $E_{THz,pk}$ for the three pump spot sizes and pump powers up to 6 W for $f_{rot} = 300$ Hz. In accordance with the quadratic terahertz power scaling, a linear scaling is observed up to a power that corresponds to a fluence of ~ 0.1 mJ/cm² [see also Fig. S4(b)]. Interestingly, in contrast to the terahertz power, $E_{THz,pk}$ is almost independent of the pump spot size for $w_p = 1.7$ mm and $w_p = 2$ mm, and it decreases only slightly for $w_p = 3.7$ mm. This behavior can be understood by considering that the higher terahertz power emitted at small pump spot size (i.e., at higher fluence) is compensated by the reduced terahertz beam diameter and the resulting larger terahertz focus at the detector, as sketched in the inset of Fig. 3(c) and as qualitatively supported by a simplified calculation in the supplementary material. This finding indicates that for the smaller spot sizes, the terahertz pulses propagate through the setup without major aperture losses and that the terahertz beam is slightly clipped at optical elements for the largest pump beam, as also evident from the larger horizontal width of the terahertz focus [inset of Fig. 4(c)].

The results in Fig. 3 show that for a given pump power, smaller spot sizes and higher fluences are advantageous for achieving higher terahertz powers. However, when high terahertz fields are required at low terahertz power, such as in THz-STM, larger pump spot sizes are advantageous as long as the terahertz beam propagates through the setup without clipping. The optimal condition for achieving the highest FCE and terahertz peak fields is obtained for pump spot sizes that ensure an excitation fluence of ~ 0.5–1 mJ/cm², where the PCE is maximum [Fig. S4(a)], and using a telescope with a magnification that allows the full aperture of the setup to be used. However, a critical limit is reached when the beam size becomes comparable to the wavelength of the lower terahertz frequencies within the STE spectrum. In this case, low and high terahertz frequencies propagate at drastically different divergence angles, making broadband collection and collimation of the pulses difficult (see supplementary material in Ref. 34). Together with

the single-pulse saturation limit imposed by the fluence,[23] this behavior will limit the performance of the STE at smaller pump spot sizes.

Finally, we quantify the terahertz electric-field amplitudes available for experiments using the rotating STE for pump powers up to 18 W and at two different repetition rates of 1 and 2 MHz for $2w_p = 3.7$ and 1.7 mm, respectively. We determine the terahertz peak field by[2,24,35]

$$E_{THz,pk} = \sqrt{\frac{W_{THz}Z_0/n}{(\pi/4\ln 2)f_x f_y \int dt \left|\hat{E}_{THz}(t)\right|^2}}, \quad (1)$$
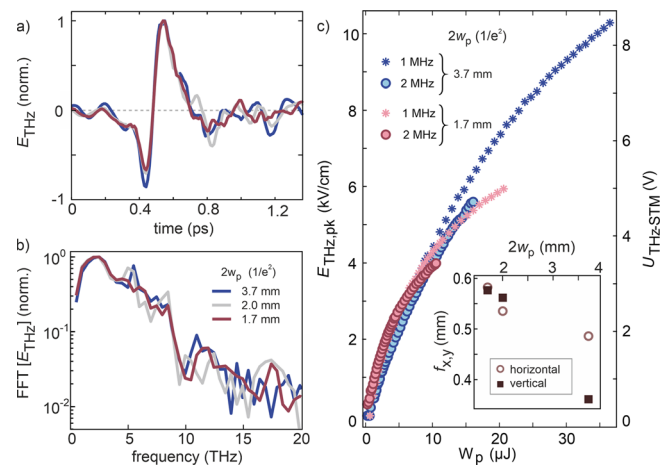

FIG. 4. Quantification of the terahertz electric field at the EOS position for two repetition rates and pump spot sizes. (a) Normalized terahertz electric-field waveforms and (b) corresponding terahertz spectra for $f_{rep} = 2$ MHz. (c) Dependence of the terahertz peak electric field (left ordinate) and terahertz peak bias in the STM (right ordinate) on the pump pulse energy. Inset: dependence of terahertz beam size (f_x, f_y) on pump spot size. In all panels, $f_{rot} = 300$ Hz.

where Z_0 is the vacuum impedance, f_x and f_y are the intensity full width at half maxima (FWHM) of the terahertz focus in x and y direction, $W_{THz} = P_{THz}/f_{rep}$ is the terahertz pulse energy at the EOS position, f_{rep} is the repetition rate, and $\hat{E}_{THz}(t)$ is the electric field of a single terahertz pulse with the peak normalized to one. Note that, unlike $P_{THz,STE}$ in Fig. 3(a), P_{THz} is the terahertz power at the EOS position and not at the STE. We measure the terahertz spot size at the EOS position by the knife-edge method and f_x and f_y are shown in the inset of Fig. 4(c). We confirm that the values for $E_{THz,pk}$ obtained by Eq. (1) are in reasonable agreement with those obtained from calibration of the balanced detection signal in EOS (see the supplementary material).

Figures 4(a) and 4(b) show the normalized terahertz field waveforms $E_{THz}(t)$ and their frequency spectra obtained by deconvoluting the EOS signal with the ZnTe detector response. Figure 4(c) shows the scaling of $E_{THz,pk}$ (left ordinate) with pump-pulse energy W_p. At the highest available W_p of about 36 μJ at 1 MHz, we achieve a terahertz peak field of $\sim$10 kV/cm. Note that, at $2w_p = 1.7$ mm, we did not use the full available power to limit the fluence and avoid laser-pulse-induced optical damage.[36]

Without saturation effects and aperture losses, we expect a constant $E_{THz,pk}$ for constant W_p independent of the pump fluence. Figure 4(c) confirms the expected behavior in the limit of small pulse energies. For low W_p up to few microjoules, $E_{THz,pk}$ scales linearly with W_p with a conversion factor that is independent of f_{rep} and $2w_p$. At higher pulse energies, a sub-linear scaling is observed that is slightly more pronounced at 2 MHz, which we ascribe to residual pulse-to-pulse accumulation effects. At $f_{rot} = 300$ Hz and 2 MHz, about 6600 pulses arrive at the STE during one revolution, and the STE rotates by an arc length of $\approx$17 μm between two consecutive pulses. Thus, $\approx$100 ($\approx$215) pulses arrive in an excited area of 1.7 mm (3.7 mm) before a completely "fresh" STE region moves into the pump spot. This condition appears to be sufficient to cause accumulation effects. Its understanding requires detailed knowledge of the heat transport within the STE, which is beyond the scope of this work. A higher rotational speed in the kilohertz range combined with a larger STE should allow for a complete elimination of accumulative heating effects by operating the STE in the megahertz single-pulse regime.

Figure 4(c) (right ordinate) shows the terahertz peak bias voltage U_{THz} that is induced between the STM tip and a metallic sample. The calibration of U_{THz} is described in previous work and in the supplementary material.[11,30] The rotating STE allows us to generate peak terahertz bias voltages up to $\approx$6.2 V for the tungsten tip used in this work, and we find a conversion factor of $\sim$0.6 V/(kV/cm) similar to previously reported values.[14] We emphasize that we achieve several volts terahertz bias in the STM at terahertz pulse energies of few 10 pJ, much lower compared to similar setups using LiNbO$_3$. This is advantageous for heat-sensitive field-driven applications such as THz-STM and demonstrates the high quality of the terahertz focus and terahertz beam emitted by the STE.

In conclusion, we demonstrate a rotating STE operating at high pump powers and high repetition rates, resulting in power densities of up to 925 W/cm^2 that would lead to irreversible damage of the STE without rotation. At the highest power density used in this work (10.5 W at 1.7 mm pump beam diameter), no degradation of the STE is observed. Stable operation with no measurable fluctuations during rotation is enabled by the large-area homogeneity of the thin-film

growth used for STE fabrication. We find that rotational frequencies of a few 100 Hz are sufficient to significantly reduce the temperature increase in the pumped region of the STE. This is enabled by distributing the absorbed power over a large annulus, thereby reducing the local absorbed power density. Importantly, our approach allows to excite the STE by laser pulses of several 10 μJ energy within a beam of few millimeters diameter at megahertz repetition rates, facilitating STE operation at optimal fluences of $\sim$0.1–1 mJ/cm^2 at such laser parameters. The rotating STE is of particular interest for field-driven terahertz applications that require high repetition rates and reasonably high terahertz fields, for example, THz-STM, where it can compete with standard single-cycle terahertz sources such as LiNbO$_3$. Furthermore, the design is scalable, and using a larger STE and faster rotational speeds, it should allow STE operation at much higher pump powers up to the kilowatt level.

See the supplementary material for details on (1) terahertz power calibration; (2) thermal radiation; (3) terahertz power scaling; (4) power conversion efficiency at STE; (5) electro-optic sampling; (6) dependence of the terahertz electric field on pump spot size; (7) terahertz bias calibration in STM; and (8) stability of the rotating STE.

AUTHOR DECLARATIONS
Conflict of Interest

Yes, Tom S. Seifert and Tobias Kampfrath are shareholders of TeraSpinTec GmbH, and Tom S. Seifert is an employee of TeraSpinTec GmbH.

Author Contributions

Alkisti Vaitsi: Formal analysis (lead); Investigation (lead); Methodology (equal); Visualization (lead); Writing – original draft (equal); Writing – review & editing (equal). **Vivien Sleziona:** Investigation (supporting); Methodology (equal); Writing – review & editing (supporting). **Luis E. Parra López:** Formal analysis (supporting); Investigation (supporting); Methodology (supporting); Writing – review & editing (supporting). **Yannic Behovits:** Formal analysis (supporting); Resources (supporting); Writing – review & editing (supporting). **Fabian Schulz:** Methodology (supporting); Writing – review & editing (supporting). **Natalia Martín Sabanés:** Methodology (supporting); Writing – review & editing (supporting). **Tobias Kampfrath:** Resources (supporting); Writing – original draft (supporting); Writing – review & editing (equal). **Martin Wolf:** Project administration (supporting); Supervision (supporting); Writing – review & editing (supporting). **Tom S. Seifert:** Resources (supporting); Writing – original draft (supporting); Writing – review & editing (equal). **Melanie Müller:** Conceptualization (lead); Formal analysis (supporting); Methodology

DATA AVAILABILITY

The data that support the findings of this study are available from the corresponding author upon reasonable request.

REFERENCES

[1] T. Seifert, S. Jaiswal, U. Martens, J. Hannegan, L. Braun, P. Maldonado, F. Freimuth, A. Kronenberg, J. Henrizi, I. Radu, E. Beaurepaire, Y. Mokrousov, P. M. Oppeneer, M. Jourdan, G. Jakob, D. Turchinovich, L. M. Hayden, M. Wolf, M. Münzenberg, M. Kläui, and T. Kampfrath, "Efficient metallic spintronic emitters of ultrabroadband terahertz radiation," Nat. Photonics **10**(7), 483–488 (2016).

[2] R. Rouzegar, A. L. Chekhov, Y. Behovits, B. R. Serrano, M. A. Syskaki, C. H. Lambert, D. Engel, U. Martens, M. Münzenberg, M. Wolf, G. Jakob, M. Kläui, T. S. Seifert, and T. Kampfrath, "Broadband spintronic terahertz source with peak electric fields exceeding 1.5 MV/cm," Phys. Rev. Appl. **19**(3), 034018 (2023).

[3] T. Seifert, S. Jaiswal, M. Sajadi, G. Jakob, S. Winnerl, M. Wolf, M. Kläui, and T. Kampfrath, "Ultrabroadband single-cycle terahertz pulses with peak fields of 300 kV cm-1 from a metallic spintronic emitter," Appl. Phys. Lett. **110**(25), 252402 (2017).

[4] T. S. Seifert, L. Cheng, Z. Wei, T. Kampfrath, and J. Qi, "Spintronic sources of ultrashort terahertz electromagnetic pulses," Appl. Phys. Lett. **120**(18), 180401 (2022).

[5] E. T. Papaioannou and R. Beigang, "THz spintronic emitters: A review on achievements and future challenges," Nanophotonics **10**(2), 1243–1257 (2021).

[6] M. T. Hibberd, D. S. Lake, N. A. B. B. Johansson, T. Thomson, S. P. Jamison, and D. M. Graham, "Magnetic-field tailoring of the terahertz polarization emitted from a spintronic emitter," Appl. Phys. Lett. **114**(3), 031101 (2019).

[7] D. Kong, X. Wu, B. Wang, T. Nie, M. Xiao, C. Pandey, Y. Gao, L. Wen, W. Zhao, C. Ruan, J. Miao, Y. Li, and L. Wang, "Broadband spintronic terahertz emitter with magnetic-field manipulated polarizations," Adv. Opt. Mater. **7**(20), 1900487 (2019).

[8] H. Niwa, N. Yoshikawa, M. Kawaguchi, M. Hayashi, and R. Shimano, "Switchable generation of azimuthally- and radially-polarized terahertz beams from a spintronic terahertz emitter," Opt. Express **29**(9), 13331 (2021).

[9] R. I. Herapath, S. M. Hornett, T. S. Seifert, G. Jakob, M. Kläui, J. Bertolotti, T. Kampfrath, and E. Hendry, "Impact of pump wavelength on terahertz emission of a cavity-enhanced spintronic trilayer," Appl. Phys. Lett. **114**(4), 041107 (2019).

[10] T. L. Cocker, V. Jelic, R. Hillenbrand, and F. A. Hegmann, "Nanoscale terahertz scanning probe microscopy," Nat. Photonics **15**(8), 558–569 (2021).

[11] M. Müller, N. Martín Sabanés, T. Kampfrath, and M. Wolf, "Phase-resolved detection of ultrabroadband THz pulses inside a scanning tunneling microscope junction," ACS Photonics **7**(8), 2046–2055 (2020).

[12] N. Martín Sabanés, F. Krecinic, T. Kumagai, F. Schulz, M. Wolf, and M. Müller, "Femtosecond thermal and nonthermal hot electron tunneling inside a photo-excited tunnel junction," ACS Nano **16**(9), 14479–14489 (2022).

[13] M. Eisele, T. L. Cocker, M. A. Huber, M. Plankl, L. Viti, D. Ercolani, L. Sorba, M. S. Vitiello, and R. Huber, "Ultrafast multi-terahertz nano-spectroscopy with sub-cycle temporal resolution," Nat. Photonics **8**(11), 841–845 (2014).

[14] M. Abdo, S. Sheng, S. Rolf-Pissarczyk, L. Arnhold, J. A. J. Burgess, M. Isobe, L. Malavolti, and S. Loth, "Variable repetition rate THz source for ultrafast scanning tunneling microscopy," ACS Photonics **8**(3), 702–708 (2021).

[15] J. Allerbeck, J. Kuttruff, L. Bobzien, L. Huberich, M. Tsarev, and B. Schuler, "Efficient and continuous carrier-envelope phase control for terahertz lightwave-driven scanning probe microscopy," ACS Photonics **10**(11), 3888–3895 (2023).

[16] C. J. Saraceno, "Mode-locked thin-disk lasers and their potential application for high-power terahertz generation," J. Opt. **20**(4), 044010 (2018).

[17] F. Röser, J. Rothhard, B. Ortac, A. Liem, O. Schmidt, T. Schreiber, J. Limpert, and A. Tünnermann, "131 W 220 fs fiber laser system," Opt. Lett. **30**(20), 2754 (2005).

[18] A. Giesen, H. Hügel, A. Voss, K. Wittig, U. Brauch, and H. Opower, "Scalable concept for diode-pumped high-power solid-state lasers," Appl. Phys. B **58**(5), 365–372 (1994).

[19] C.-H. Lu, W.-H. Wu, S.-H. Kuo, J.-Y. Guo, M.-C. Chen, S.-D. Yang, and A. H. Kung, "Greater than 50 times compression of 1030 nm Yb:KGW laser pulses to single-cycle duration," Opt. Express **27**(11), 15638 (2019).

[20] C. H. Lu, W. H. Wu, S. H. Kuo, Y. H. Tseng, C. L. Tsai, M. C. Chen, A. H. Kung, and S. D. Yang, "Generation of octave-spanning intense supercontinuum from Yb: Doped solid-state lasers in multiple thin plates," in Optics InfoBase Conference Papers, 2017.

[21] A.-L. Viotti, M. Seidel, E. Escoto, S. Rajhans, W. P. Leemans, I. Hartl, and C. M. Heyl, "Multi-pass cells for post-compression of ultrashort laser pulses," Optica **9**(2), 197 (2022).

[22] T. Okamoto, Y. Kunihashi, Y. Shinohara, H. Sanada, M.-C. Chen, and K. Oguri, "Operation at 1 MHz of 1.7-cycle multiple plate compression at 35-W average output power," Opt. Lett. **48**(10), 2579 (2023).

[23] T. Vogel, A. Omar, S. Mansourzadeh, F. Wulf, N. M. Sabanés, M. Müller, T. S. Seifert, A. Weigel, G. Jakob, M. Kläui, I. Pupeza, T. Kampfrath, and C. J. Saraceno, "Average power scaling of THz spintronic emitters efficiently cooled in reflection geometry," Opt. Express **30**(12), 20451 (2022).

[24] T. O. Buchmann, E. J. Railton Kelleher, M. Jazbinsek, B. Zhou, J. H. Seok, O. P. Kwon, F. Rotermund, and P. U. Jepsen, "High-power few-cycle THz generation at MHz repetition rates in an organic crystal," APL Photonics **5**(10), 106103 (2020).

[25] F. Meyer, N. Hekmat, T. Vogel, A. Omar, S. Mansourzadeh, F. Fobbe, M. Hoffmann, Y. Wang, and C. J. Saraceno, "Milliwatt-class broadband THz source driven by a 112 W, sub-100 fs thin-disk laser," Opt. Express **27**(21), 30340 (2019).

[26] F. Meyer, T. Vogel, S. Ahmed, and C. J. Saraceno, "Single-cycle, MHz repetition rate THz source with 66 mW of average power," Opt. Lett. **45**(9), 2494 (2020).

[27] P. L. Kramer, M. K. R. Windeler, K. Mecseki, E. G. Champenois, M. C. Hoffmann, and F. Tavella, "Enabling high repetition rate nonlinear THz science with a kilowatt-class sub-100 fs laser source," Opt. Express **28**(11), 16951 (2020).

[28] F. F. Stiewe, T. Winkel, Y. Sasaki, T. Tubandt, T. Kleinke, C. Denker, U. Martens, N. Meyer, T. S. Parvini, S. Mizukami, J. Walowski, and M. Münzenberg, "Spintronic emitters for super-resolution in THz-spectral imaging," Appl. Phys. Lett. **120**(3), 32406 (2022).

[29] S. C. Chen, Z. Feng, J. Li, W. Tan, L. H. Du, J. Cai, Y. Ma, K. He, H. Ding, Z. H. Zhai, Z. R. Li, C. W. Qiu, X. C. Zhang, and L. G. Zhu, "Ghost spintronic THz-emitter-array microscope," Light Sci. Appl. **9**(1), 2047–7538 (2020).

[30] S. Yoshida, H. Hirori, T. Tachizaki, K. Yoshioka, Y. Arashida, Z. H. Wang, Y. Sanari, O. Takeuchi, Y. Kanemitsu, and H. Shigekawa, "Subcycle transient scanning tunneling spectroscopy with visualization of enhanced terahertz near field," ACS Photonics **6**(6), 1356–1364 (2019).

[31] Q. Wu and X. C. Zhang, "7 terahertz broadband GaP electro-optic sensor," Appl. Phys. Lett. **70**(14), 1784–1786 (1997).

[32] A. Leitenstorfer, S. Hunsche, J. Shah, M. C. Nuss, and W. H. Knox, "Detectors and sources for ultrabroadband electro-optic sampling: Experiment and theory," Appl. Phys. Lett. **74**(11), 1516–1518 (1999).

[33] T. Kampfrath, J. Nötzold, and M. Wolf, "Sampling of broadband terahertz pulses with thick electro-optic crystals," Appl. Phys. Lett. **90**(23), 231113 (2007).

[34] T. S. Seifert, N. M. Tran, O. Gueckstock, S. M. Rouzegar, L. Nadvornik, S. Jaiswal, G. Jakob, V. V. Temnov, M. Münzenberg, M. Wolf, M. Kläui, and T. Kampfrath, "Terahertz spectroscopy for all-optical spintronic characterization of the spin-Hall-effect metals Pt, W and Cu80Ir20," J. Phys. D: Appl. Phys. **51**(36), 364003 (2018).

[35] M. Sajadi, M. Wolf, and T. Kampfrath, "Terahertz-field-induced optical birefringence in common window and substrate materials," Opt. Express **23**(22), 28985 (2015).

[36] S. Kumar, A. Nivedan, A. Singh, Y. Kumar, P. Malhotra, M. Tondusson, E. Freysz, and S. Kumar, "Optical damage limit of efficient spintronic THz emitters," IScience **24**(10), 103152 (2021).